



NRC Publications Archive Archives des publications du CNRC

Fracture load predictions and measurements for toughened epoxy adhesive joints

Azari, S.; Eskandarian, M.; Papini, M.; Schroeder, J. A.; Spelt, J. K.

This publication could be one of several versions: author's original, accepted manuscript or the publisher's version. / La version de cette publication peut être l'une des suivantes : la version prépublication de l'auteur, la version acceptée du manuscrit ou la version de l'éditeur.

For the publisher's version, please access the DOI link below. / Pour consulter la version de l'éditeur, utilisez le lien DOI ci-dessous.

Publisher's version / Version de l'éditeur:

<https://doi.org/10.1016/j.engfracmech.2009.05.011>

Journal of Engineering Fracture Mechanics, 76, 13, pp. 2039-2055, 2009-05-28

NRC Publications Record / Notice d'Archives des publications de CNRC:

<https://nrc-publications.canada.ca/eng/view/object/?id=f0202d53-3cee-4fb4-ab16-06249c85a605>

<https://publications-cnrc.canada.ca/fra/voir/objet/?id=f0202d53-3cee-4fb4-ab16-06249c85a605>

Access and use of this website and the material on it are subject to the Terms and Conditions set forth at

<https://nrc-publications.canada.ca/eng/copyright>

READ THESE TERMS AND CONDITIONS CAREFULLY BEFORE USING THIS WEBSITE.

L'accès à ce site Web et l'utilisation de son contenu sont assujettis aux conditions présentées dans le site

<https://publications-cnrc.canada.ca/fra/droits>

LISEZ CES CONDITIONS ATTENTIVEMENT AVANT D'UTILISER CE SITE WEB.

Questions? Contact the NRC Publications Archive team at

PublicationsArchive-ArchivesPublications@nrc-cnrc.gc.ca. If you wish to email the authors directly, please see the first page of the publication for their contact information.

Vous avez des questions? Nous pouvons vous aider. Pour communiquer directement avec un auteur, consultez la première page de la revue dans laquelle son article a été publié afin de trouver ses coordonnées. Si vous n'arrivez pas à les repérer, communiquez avec nous à PublicationsArchive-ArchivesPublications@nrc-cnrc.gc.ca.





Contents lists available at ScienceDirect

Engineering Fracture Mechanics

journal homepage: www.elsevier.com/locate/engfracmech

Fracture load predictions and measurements for highly toughened epoxy adhesive joints

S. Azari^a, M. Eskandarian^b, M. Papini^c, J.A. Schroeder^d, J.K. Spelt^{a,*}^a Department of Mechanical and Industrial Engineering, University of Toronto, 5 King's College Road, Toronto, Ontario, Canada M5S 3G8^b Aluminium Technology Centre, Industrial Materials Institute, National Research Council Canada (ATC/IMI/NRC), 501 boul. de l'Université, Chicoutimi, Québec, Canada G7H 8C3^c Department of Mechanical and Industrial Engineering, Ryerson University, 350 Victoria Street, Toronto, Ontario, Canada M5B 2K3^d GM Research and Development, 30500 Mound Road, Warren, MI 48090-9055, USA

ARTICLE INFO

Article history:

Received 15 December 2008

Received in revised form 14 May 2009

Accepted 22 May 2009

Available online xxxx

Keywords:

Adhesive joints

Strength prediction

Mixed-mode fracture

R-curve

Toughened epoxy

ABSTRACT

A method to predict the ultimate strength of adhesive joints has been evaluated for the quasi-static loading of a variety of cracked-lap shear (CLS) and single-lap shear (SLS) joints bonded with a high-strength, toughened epoxy adhesive. The adhesive strength was experimentally characterized in terms of the steady-state critical strain energy release rate, G_c^s , as a function of the loading phase angle, using double cantilever beam (DCB) joints. Comparing the calculated energy release rate using the J -integral with the G_c^s at the corresponding phase angle, the ultimate failure load in the fracture joint was predicted and compared with experimental results. When the toughening of the adhesive during subcritical crack growth (i.e. its R -curve behavior) was considered in the analysis, good agreement between the predicted and experimental failure loads was achieved, both for joints made with aluminum or steel adherends. The initial condition at the end of joint overlap (fillet or pre-crack) did not affect the ultimate joint strength because of the significant amount of subcritical crack growth.

© 2009 Elsevier Ltd. All rights reserved.

1. Introduction

A variety of strain and stress-based failure criteria have been proposed to predict the strength of adhesive joints [1–5]. The maximum stresses at the end of the joint overlap are difficult to predict accurately, and consequently it has been proposed that failure can be based on the integral of stress over some characteristic length [5,6]. A related critical stress/strain approach based on finite element modeling assumes that an adhesive joint fails when a “damage zone” extending from the end of the joint overlap reaches a specific value. This critical size and the adhesive failure criterion governing the development of the damage zone are calibrated by comparison with the measured failure loads on joints that mimic those used in the application of interest [7,8]. These approaches have been used to predict the strengths of joints when cracking first appears at the end of the overlap, rather than the ultimate strength of joints.

Another finite element approach is cohesive zone modeling, which has been used, for example, to predict failure loads in single-lap shear joints (elastic and plastically deforming) [9,10]. The approach attempts to mimic the global deformation and stress in the damage zone at the tip of a developing crack, and involves the selection of traction–separation parameters that achieve this in mode I and mode II. However, the choice of these parameters is based largely on trial and error, and will not be unique in general (i.e. experimental results can be matched with more than one set of parameters). Moreover, the

* Corresponding author. Tel.: +1 416 9785435; fax: +1 416 9787753.

E-mail address: spelt@mie.utoronto.ca (J.K. Spelt).

Nomenclature

a	crack length
D	flexural rigidity per unit width
E	elastic modulus of adherend
E_a	elastic modulus of adhesive
F	actuator force in DCB testing
F_1	applied force on the upper loading pin of a DCB
F_2	applied force on the lower loading pin of a DCB
G	strain energy release rate
G_I	mode I strain energy release rate
G_{IC}	mode I critical strain energy release rate
G_{II}	mode II strain energy release rate
G_{IIC}	mode II critical strain energy release rate
G_a	shear modulus of adhesive
G_c	critical strain energy release rate
G_c^i	crack initiation strain energy release rate
G_c^s	steady-state critical strain energy release rate
h	adherend thickness
M	bending moment per unit width
P	axial force per unit width in the beam
P_{Exp}	experimental failure load per unit width
P_i	crack initiation force per unit width
P_{Pred}	predicted failure load per unit width
t	adhesive thickness
v	beam deflection

Greek symbols

α	calibration constant
ψ	phase angle

sensitivity of the strength prediction to a given traction–separation law parameter must be assessed for each joint geometry [11], and numerical instabilities can affect finite element solutions involving cohesive zone models [12].

For joints in which the adherends remain elastic, an analytical fracture-based method has been shown to accurately predict the final fracture loads of joints bonded with relatively brittle epoxy adhesives [13–17]. This approach was based on characterizing the strength of an adhesive system using a fracture envelope; i.e. the steady-state critical strain energy release rate as a function of the loading phase angle. The energy release rate for a particular joint was calculated using a closed-form expression for the J -integral in a cracked adhesive sandwich. The calculated energy release rate and phase angle for the joint were then compared to the steady-state critical strain energy release rate, G_c^s , at the corresponding phase angle ψ . The experimentally measured fracture envelope was used and the fracture load was extracted. This approach was shown to accurately predict the ultimate loads of joints made with two relatively brittle epoxy adhesives of moderate strength bonded to aluminum adherends [16].

The objective of the present work was to assess the performance of this approach with an epoxy adhesive that was an order of magnitude tougher than those used in earlier work. The adhesive also displayed a much more prominent R -curve, compared to the previously tested brittle adhesives [14,16], and it was not obvious that the critical strain energy release rate could still form an appropriate failure criterion. Joint strength was predicted using the measured fracture envelope, $G_c^s(\psi)$, and compared with measured fracture loads for two commonly used joints, the cracked-lap shear (CLS) and the single-lap shear (SLS), made with either steel or aluminum adherends.

2. Specimen preparation

The fracture envelope was measured using double cantilever beam (DCB) specimens fabricated from 12.7 mm × 19.05 mm (1/2" × 3/4") AA6061-T651 flat bars (yield stress $\sigma_y = 275$ MPa), and having a bondline thickness of 0.4 mm, controlled by placing spacing wires in the bondline. Prior to bonding, the aluminum adherends were abraded using a silicon carbide nylon mesh abrasive pad which gave an average roughness of $R_a = 0.77 \pm 0.02$ μm . The aluminum bars were then pretreated using the P2 etching process [18]. By inserting a thermocouple in the bondline, the adhesive temperature was monitored during cure to ensure that the adhesive remained at 180 °C for 30 min, the manufacturer recommended curing schedule. Cracked-lap shear (CLS) and single-lap shear (SLS) joints were made from AA7075-T651, $\sigma_y = 500$ MPa, in order to prevent yielding of the adherends during the fracture tests. The surface preparation and the curing procedure were as with

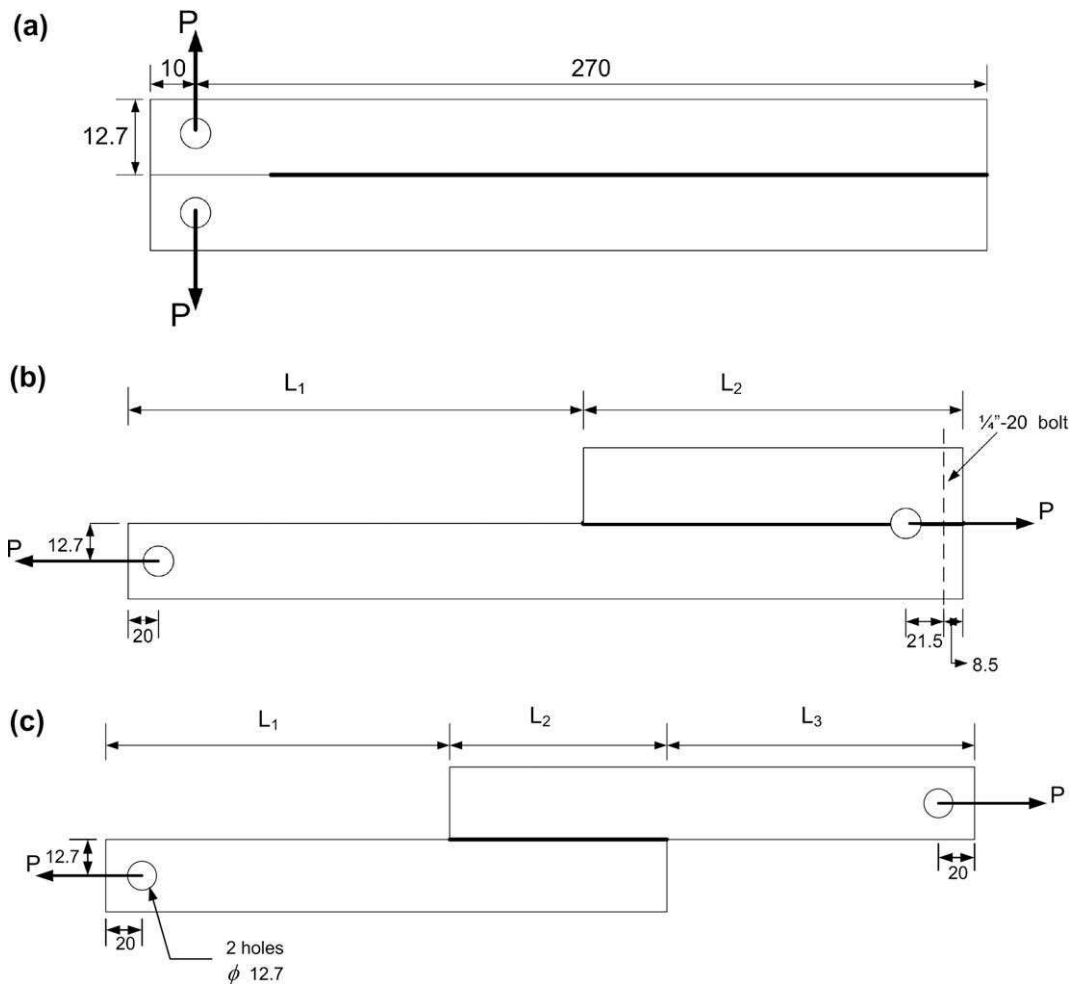


Fig. 1. Nomenclature and geometry of (a) DCB, (b) CLS and (c) SLS joints. All dimensions in mm, unless stated.

the DCB joints. To remove the excessive adhesive after curing and achieve a specimen of uniform width, the sides of the joints were carefully milled to avoid edge damage and overheating. To improve the visibility of the crack, the bondline was then sanded with P100 sandpaper, and a thin coating of diluted correction fluid was applied. The geometries of the DCB, CLS and SLS joints are shown schematically in Fig. 1. As explained below, the CLS specimens were used with several end configurations: one that had a foil precrack and two that had adhesive fillets and no precrack.

To evaluate the failure load prediction technique with another system, DCB, CLS and SLS specimens were also manufactured from AISI 4140 flat steel bars. The bars were first abraded with an aluminum oxide abrasive pad, giving an average roughness of $R_a = 0.85 \pm 0.03 \mu\text{m}$, followed by degreasing using acetone and ethanol. DCB specimens were manufactured from $12.7 \text{ mm} \times 19.05 \text{ mm}$ ($1/2'' \times 3/4''$) flat bars. As was the case with the aluminum joints, the bondline thickness was 0.4 mm.

3. Fracture envelope

3.1. Experimental approach

Crack growth must be measured over a range of mode ratios (phase angles) in order to obtain the fracture envelope (G_c^S vs. phase angle) for a given adhesive system, defined as the combination of adhesive, pretreatment, adherend, bondline thickness and cure schedule. The load jig shown in Ref. [14] provides a convenient way of measuring the critical strain energy release rate, G_c , as a function of the phase angle using a single DCB specimen. By adjusting the pin locations in the link arms (Fig. 2), the load jig allows many different combinations of moments to be applied to the arms of the DCB specimen using a single actuator and specimen geometry. The load jig is statically determinate, and the specimen loads, F_1 and F_2 are given from equilibrium considerations of the link-arm system as [14]

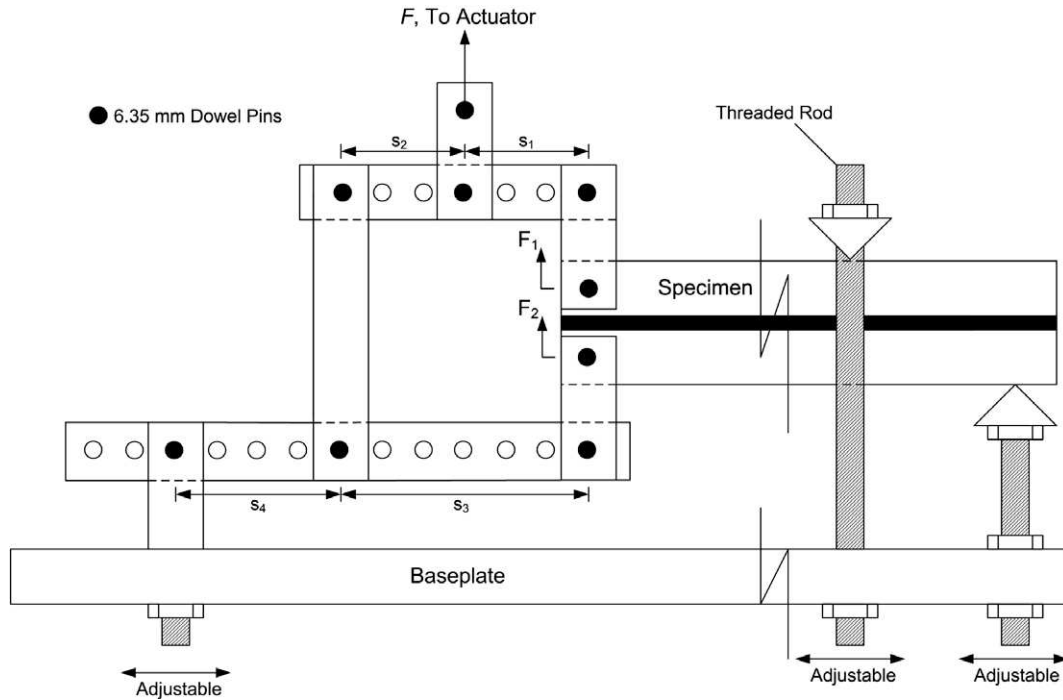


Fig. 2. Schematic illustration of the load jig [14] (not to scale). The distance between the holes on the load jig is 25.4 mm.

$$F_1 = F \left(1 - \frac{s_1}{s_3} \right) \quad (1)$$

$$F_2 = F_1 \frac{s_1}{s_2} \frac{1}{\left(1 + \frac{s_3}{s_4} \right)} \quad (2)$$

where s_1 , s_2 , s_3 and s_4 are defined in Fig. 2 as the distances between the pin centers.

A load frame with a capacity of 10 kN was used to load the specimen under displacement control. The load was increased at a constant cross-head speed of 1 mm/min. The crack length was measured from the center of the loading pins on the DCB specimens using a microscope mounted on a micrometer stage having an accuracy of 0.01 mm. The accuracy in the crack length measurement decreased as the phase angle increased, due to the less opening of the crack. However, it is believed that the accuracy in the measured crack length was always better than 0.1 mm, which incurred a very insignificant error in the measured G_c (about 0.1%). The crack front along the width of the DCB joint was fairly uniform, therefore, a crack length measurement based on the crack observed on the edge of the specimen was accurate enough for G_c measurements, and a very insignificant difference would be observed if the G calculation was based on the crack length in the middle of the specimen's width. The maximum difference between the crack at the edge of the specimen and the crack front in the middle of the specimen was measured to be about 2 mm, which, if assuming the crack length according to the middle of the specimen's width, could result in only a 2% increase in the G_c . Crack growth was stable in this system so that many crack extension events could be recorded with a single specimen.

Refs. [14] and [16] describe the procedure to measure the fracture envelope for two relatively brittle single-part epoxy adhesives. For those adhesives, it was appropriate to start and stop the cross-head displacement repeatedly until new cracking was observed in the damage zone ahead of the macro-crack at the critical load for the measured crack length. However, the single-part, heat-cured toughened epoxy adhesive used in the present study was found to be much tougher and more visco-elastic than those two adhesives, and therefore the crack growth was less abrupt, being more of a gradual tearing of the bondline. Consequently, relying solely on visual observation of the damage zone while manually starting and stopping the cross-head iteratively, led to overloading the specimen and recording loads greater than the true critical load corresponding to G_c . In principle, this problem could be resolved by choosing a very small cross-head speed; however, a small cross-head speed would greatly increase the test duration, and due to the visco-elastic nature of the adhesive, creep crack growth might occur at loads below that corresponding to G_c . For the present very tough adhesive system, a better approach was to start and stop the cross-head displacement repeatedly in the vicinity of the expected fracture load (each time at a constant cross-head speed of 1.0 mm/min) until a drop in the applied load was observed. This maximum load prior to the drop was taken as the critical fracture load for the measured crack length if visual inspection through the microscope confirmed that the macro-crack had propagated. After measuring the new macro-crack length, the DCB was unloaded and the same procedure was followed again beginning at the new crack length. In this way many G_c measurements could be obtained

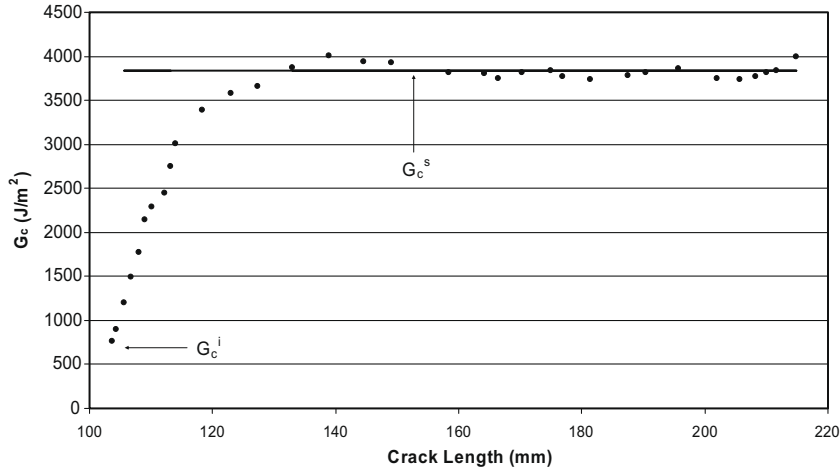


Fig. 3. Typical R-curve behavior of a DCB joint. Aluminum specimen tested at a phase angle of $\psi = 27^\circ$.

for a single DCB. Although this measurement procedure differed from that utilized in [13–17], where the crack tip was considered as the furthest advanced micro-crack, there was a negligible effect on the steady state G_c beyond the rising part of the R-curve (Fig. 3), since the length of the damage zone was usually small compared to the overall crack length. For instance, for a specimen tested at a loading phase angle of 16° , such a difference in crack tip definition resulted in only a 2–4% reduction in the calculated G_c .

3.2. DCB data analysis, G calculation and mode partitioning

The calculation of the phase angle and critical energy release rate, G_c , of DCB specimens has been done using beam theory [14] or a beam-on-elastic foundation approach [19]. The beam theory approach neglects the presence of the adhesive, while the beam-on-elastic-foundation model accounts for the additional compliance of the adhesive layer.

3.2.1. Beam theory [14]

Assuming that the adhesive layer of the test specimen is thin, and neglecting shear deformation, the energy release rate per unit area of crack extension, G , and the nominal phase angle (mode ratio) of loading, $\psi = \arctan \left(\sqrt{G_{II}/G_I} \right)$, can be expressed as

$$G = \frac{(F_1 a)^2}{2D} \left[1 + \left(\frac{F_2}{F_1} \right)^2 - \frac{1}{8} \left(1 + \left(\frac{F_2}{F_1} \right)^2 \right)^2 \right] \quad (3)$$

$$\psi = \arctan \left[\frac{\sqrt{3}}{2} \frac{\left(\frac{F_1}{F_2} + 1 \right)}{\left(\frac{F_1}{F_2} - 1 \right)} \right] \quad (4)$$

where a is the crack length measured from the loading pins and D is the flexural rigidity per unit width of the adherends, given under plane stress by

$$D = \frac{Eh^3}{12} \quad (5)$$

with E and h being the Young's modulus and thickness of the adherends, respectively. Note that the loads are positive in the direction of actuator force, F , as depicted in Fig. 2, and that F_1 and F_2 in Eq. (3) are also defined per unit width and are, respectively, the forces at the upper and lower loading pins of the specimen. From Eq. (2) it is seen that the ratio F_1/F_2 is only a function of the chosen load jig geometry (s_1, s_2, s_3 and s_4), and hence the nominal phase angle of loading (Eq. (4)) is independent of the crack length, a , of the specimen. s_1, s_2, s_3, s_4 are defined positive as shown in Fig. 2.

3.2.2. Beam-on-elastic-foundation model

An analytical beam-on-elastic-foundation model for the DCB energy release rate has been presented [19]. If F_1 and F_2 (Fig. 2) are transformed to f_1 and f_2 through the equations

$$\begin{aligned} f_1 &= \frac{F_1 - F_2}{2} \\ f_2 &= -\frac{F_1 + F_2}{2} \end{aligned} \quad (6)$$

then the energy release rate in an adhesive with a thickness t is given by

$$G = \frac{12a^2}{E(h-t)^3} \left[f_1^2 \Phi_I^2 + \frac{3}{4} f_2^2 \Phi_{II}^2 \right] \quad (7)$$

where a is the crack length, and E and h are, respectively, the elastic modulus and thickness of the adherends. Φ_I and Φ_{II} are given by

$$\Phi_I = 1 + 0.667 \frac{h}{a} \left[(1 - t/h)^3 [1 + t/h(2E/E_a - 1)] \right]^{0.25}$$

$$\Phi_{II} = 1 + 0.206 \frac{h}{a} \sqrt{\left[1 - \frac{t}{h} \right] \left[1 + \frac{2tE\alpha}{G_a h} \right]} \quad (8)$$

where $\alpha = 2.946$ is a calibration constant that was determined using a finite element analysis [19]. E_a and G_a are the elastic and shear modulus of the adhesive, respectively. The phase angle is given by

$$\psi = \arctan \left[\frac{\sqrt{3} F_2 \Phi_{II}}{2 F_1 \Phi_I} \right] \quad (9)$$

3.3. Experimental results for DCB specimens

During the first several crack growth sequences, the measured critical energy release rate, G_c , increased with crack length, becoming almost constant after the crack propagated a certain distance (Fig. 3). Such resistance curves are observed commonly in the interlaminar fracture of composites and in adhesive joints [16,20–27], and result from the growth of a damage zone ahead of the crack tip, which increases the joint toughness as the volume of yielded and micro-cracked material expands. The rising portion of the R -curve ends when the damage zone, or the plastic zone, reaches a steady-state size [16,26]. The length of the rising portion of the curve increased with increasing mode ratio and with increasing bondline thickness, both of which also caused the steady-state size of the crack tip damage zone to grow. This is illustrated in Figs. 4 and 5. The steady-state critical strain energy release rate, G_c^s , at each phase angle was considered to be the average value over the “plateau” (steady state) region (Fig. 3). To measure the length of the rising part of the R -curve, the starting point was the tip of the aluminum foil precrack. The end of the rising part was determined using an algorithm that identified the start of the plateau based on the change in the slope of $G(a)$.

Under mode I loading, the crack propagated in the mid-plane of the bondline. Increasing the phase angle resulted in a crack path which was closer to the more highly strained arm of the DCB joint, and left more shear hackles. This change in the crack path with increasing phase angle was in accordance with expectations [20,28]. The crack path in the aluminum

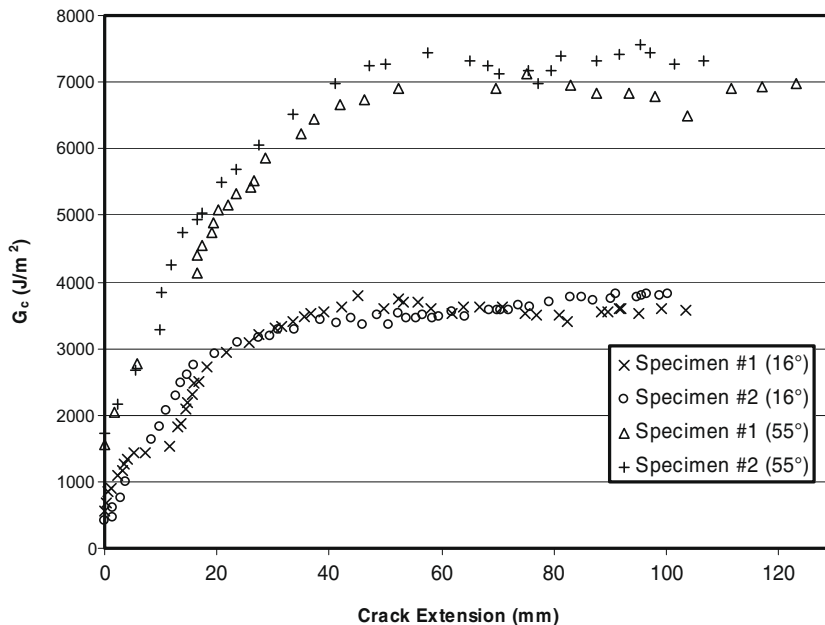


Fig. 4. G_c vs. crack length for phase angles of 16° and 55°. Two representative experiments have been shown for each phase angle. Crack extension was measured from the tip of the precrack.

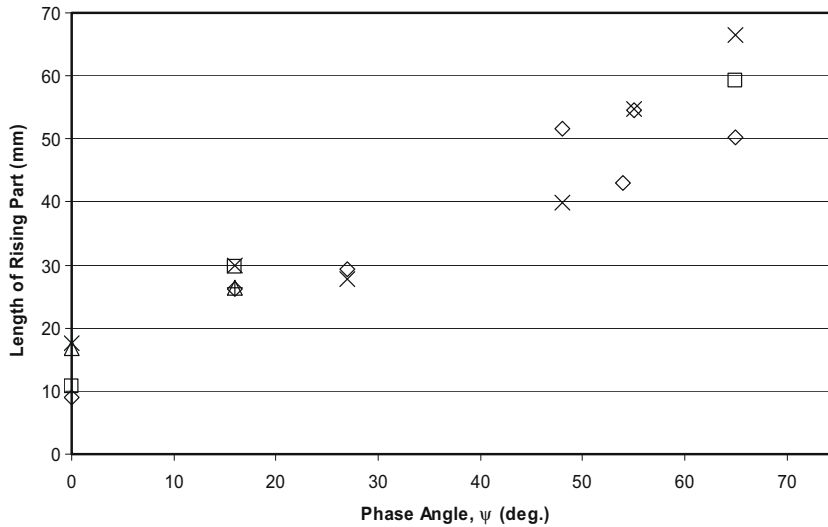


Fig. 5. Change in the length of the rising part of the R-curve, with phase angle. Different symbols are used for separate tests performed at the same phase angle.

DCB joints was fully cohesive. The steel DCBs also failed cohesively, although there were scattered small patches of interfacial failure as well. The percentage of the fracture surface that was interfacial failure for steel joints increased with phase angle, and was about 10–20% of the total fracture surface area for phase angles from 0° to 55°.

To verify that the measured G_c^s was independent of the adherend width, two specimens were made, one 19 mm (3/4") wide and the other 25.4 mm (1") wide. When tested at a phase angle, $\psi = 16^\circ$, the G_c^s values for the two specimens differed by less than 1%; therefore, a width of 19 mm was used for all specimens. The independence of the fracture behavior on specimen width over this range was also observed in [14,16]. The number of data points on the plateau region, used to measure the G_c^s , of the 19 mm and 25.4 mm wide specimens were 26 and 33, respectively.

It was of interest to investigate the effect of cross-head speed on the fracture behavior of the adhesive over a range of speeds that span typical quasi-static testing. A specimen was tested at $\psi = 16^\circ$ at a cross-head speed of 0.5 mm/min to obtain 20 G_c^s data points on the plateau. The test was then continued at a cross-head speed of 5 mm/min, and 20 more data points on the plateau were measured. The average G_c^s values for the two cross-head speeds differed by less than 3%, showing that the steady-state critical strain energy release rate was relatively insensitive to the strain rate over this range. It is expected that differences in G_c^s would be observed if a much wider range of cross-head speeds was chosen.

The fracture envelope for the aluminum adhesive system was defined by measuring G_c^s at seven different phase angles as shown in Fig. 6 (beam theory calculation). It is observed that the dependence of G_c^s on ψ was very small from $\psi = 0^\circ$ to $\psi = 30^\circ$, becoming more significant at higher phase angles, similar to what was previously reported for more brittle adhesive systems [15,16]. However, the G_c^s values were much higher than in these earlier studies. For example, the average mode I ($\psi = 0^\circ$) G_c^s for the current adhesive system was 3860 J/m² (calculated using the beam-on-elastic-foundation model), compared to 212 J/m² for Cybond 4523 GB [16] and 794 J/m² for ESP 310 adhesive [15].

A third-order polynomial was fitted to the measured fracture envelope, G_c^s vs. ψ . Eqs. (10) and (11) give the relation using the beam theory and the beam-on-elastic-foundation models, respectively:

$$G_c^s = 3237.9 + 13.342\psi - 0.6832\psi^2 + 0.0345\psi^3, \quad R^2 = 0.98 \quad (10)$$

$$G_c^s = 3850.8 + 10.996\psi - 0.9495\psi^2 + 0.0405\psi^3, \quad R^2 = 0.98 \quad (11)$$

Beam theory, which does not include the compliance of adhesive in the total joint compliance, resulted in a lower G_c^s (16% smaller at $\psi = 0^\circ$).

A commonly used equation for fitting the experimental data at different phase angles is

$$\frac{G_I}{G_{IC}} + \frac{G_{II}}{G_{IIC}} = 1 \quad (12)$$

where G_{IC} and G_{IIC} are steady-state critical energy release rates under pure mode I and pure mode II, respectively, and G_I and G_{II} are the critical components of the modes I and II energy release rates under mixed-mode crack growth conditions [29]. The measured G_I and G_{II} critical values, with the number of tested specimens and data points at the seven phase angles of Fig. 6 are listed in Table 1. The G_{IIC} at $\psi = 90^\circ$ was extrapolated from a curve fit of Fig. 6. The sixth column of Table 1 shows that the modes I and II energy release rates could be reasonably fitted using Eq. (12). The standard deviation of the steady-state critical strain energy release rate was less than 10% of the mean at each of the seven phase angles (5% on average), which was comparable to previous experience with much more brittle epoxy adhesives [14].

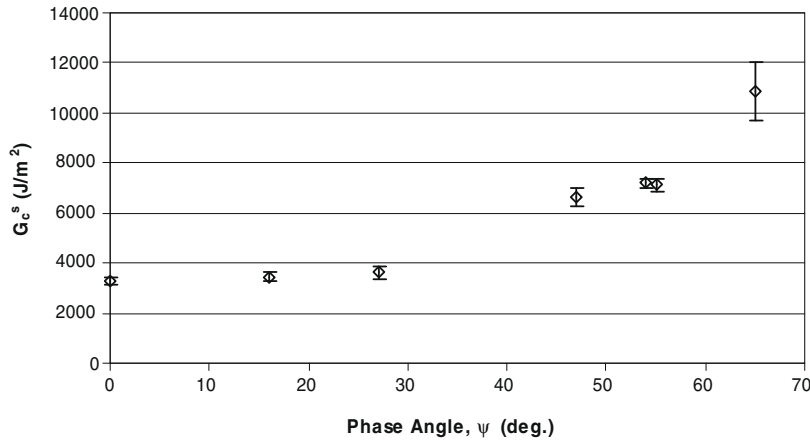


Fig. 6. Measured fracture envelope for aluminum adhesive system calculated using beam theory. Given values are average G_c^s (± 1 SD).

Table 1

Measured critical values of G_I and extrapolated G_{II} at different phase angles for the aluminum system fracture envelope. N and M represent the total number of data points and the number of specimens, respectively.

Phase angle (°)	G_I (J/m ²)		G_{II} (J/m ²)		$G_I/G_{IC} + G_{II}/G_{IIc}$	N	M
	Average	Standard deviation	Average	Standard deviation			
0	3255	151	0	0	1.0	155	4
16	3166	168	264	14	0.98	163	5
27	2842	180	767	49	0.90	44	2
48	2958	152	3668	189	1.05	25	2
54	2484	58	4699	110	0.94	14	1
55	2314	85	4821	176	0.89	29	2
65	1915	205	8978	962	0.92	46	3

A similar procedure was used to measure the fracture envelope of the steel adhesive system. The experiments were conducted at phase angles of $\psi = 0^\circ$, 16° , 27° and 48° , yielding the third-order polynomial fits given in Eqs. (13) and (14), for the beam theory and the beam-on-elastic-foundation models, respectively:

$$G_c^s = 2357.5 + 0.3847\psi + 0.1509\psi^2 + 0.0209\psi^3 \quad (13)$$

$$G_c^s = 2741.1 + 2.3884\psi + 0.1423\psi^2 + 0.0250\psi^3 \quad (14)$$

Several studies in the literature have noted an effect of substrate stiffness on the critical strain energy release rate for quasi-static fracture. Yan et al. [30] observed that the G_c^s for an adhesive system with steel adherends was less than that of the same adhesive with more flexible aluminum adherends. This was attributed to elevated stress levels in the crack tip region for the stiffer steel joint. On the other hand, Bell and Kinloch [31] compared the G_c^s of aluminum, steel and CFRP joints and found that G_c^s increased with adherend stiffness. This was attributed to the shape and the size of the plastic zone ahead of the tip and within the adhesive layer which was believed to be affected by the transverse elastic modulus of the adherends. Later however, further experiments with a similar adhesive showed that, the differences between the aluminum and steel joints were less pronounced [32], and that the differences between the CFRP and the metallic adherends were due to water absorption by the CFRP substrates. Comparing the fracture envelope of the aluminum adhesive system, Eqs. (10) and (11), with the corresponding relations for the steel adhesive system, Eqs. (13) and (14), it is observed that a slightly lower G_c^s was measured for the steel system. This was attributable to the different crack path in the steel joints, which was mostly cohesive, but had scattered small patches of interfacial failure as explained above. Overall, there was no difference that could be attributed to the modulus of the adherend material.

To predict the failure load in aluminum and steel CLS and SLS fracture joints, Eqs. (10) and (13) were considered to be the fracture envelopes of aluminum and steel systems, respectively. The reason for using the beam theory model, rather than the beam-on-elastic-foundation model, is explained in Section 4.1.

4. Quasi-static fracture tests on CLS and SLS joints

Nine CLS and eleven SLS joints of varying overlap and arm lengths were made from 25.4×19.05 mm ($1'' \times 3/4''$) flat bars of aluminum AA 7075-T651 in order to achieve a range of joint strengths to test the model predictions (Tables 2 and 3). This alloy and thickness were sufficient to prevent adherend yielding before adhesive fracture. The SLS joints had one arm longer

Table 2

Geometry and initial conditions of aluminum CLS specimens, measured crack initiation forces, P_i , and final failure loads, P_{Exp} , per unit width, compared with predicted failure loads, P_{Pred} , using a 60 mm subcritical crack length. SF, LF and P stand for small fillet, large fillet and precracked, respectively.

Specimen, initial condition	L_1, L_2 (mm)	ψ (°)	P_i (kN/m)	P_{Exp} (kN/m)	P_{Pred} (kN/m)	Error (%), $(P_{Pred} - P_{Exp})/P_{Exp}$	Displ. rate (mm/min)
C12C, SF	308, 190	51.8	2747	3787	4021	6	1.50
C4A, SF	312, 135	49.4	1299	3027	3139	4	0.25
C12B, LF	316, 152	50.1	2384	3779	3398	−10	0.35
C13C, LF	316, 130	49.3	–	3705	3063	−17	1.00
C4C, LF	234, 190	51.9	1454	4023	4085	2	0.25
C12A, P	145, 131	49.6	2598	3687	3221	−13	1.00
C13A, P	200, 150	50.3	2400	3669	3454	−6	1.00
C13B, P	330, 170	50.9	2274	3983	3681	−8	1.50
C4B, P	329, 147	50.0	1735	3855	3317	−14	0.25

Table 3

Geometry and initial conditions of aluminum SLS specimens, measured crack initiation forces, P_i , and final failure loads, P_{Exp} , per unit width, compared with predicted failure loads, P_{Pred} , using a 60 mm subcritical crack length. SF, LF and P stand for small fillet, large fillet and precracked, respectively.

Specimen, initial condition	L_1, L_2, L_3 (mm)	ψ (°)	P_i (kN/m)	P_{Exp} (kN/m)	P_{Pred} (kN/m)	Error (%), $(P_{Pred} - P_{Exp})/P_{Exp}$	Displ. rate (mm/min)
S1A, SF	197, 99, 120	47.4	2016	2277	2429	7	1.25
S1B, SF	159, 108, 82	47.2	–	2376	2370	0	0.60
S3A, SF	192, 125, 145	48.3	–	2639	2574	−2	0.20
S4A, SF	217, 87, 93	45.9	932	2011	1943	−3	0.25
S5B, SF	215, 124, 142	47.8	1279	–	–	–	0.25
S2B, LF	207, 123, 148	48.5	–	2621	2666	2	0.60
S3B, LF	158, 153, 122	48.9	–	2891	2843	−2	0.20
S4B, LF	174, 97, 102	46.6	1708	2177	2161	−1	0.25
S5C, LF	182, 115, 133	47.6	1505	2174	2445	12	0.25
S2A, P	172, 121, 143	48.6	1610	2605	2739	6	0.65
S5A, P	192, 125, 103	47.2	1924	2392	2311	−3	0.25

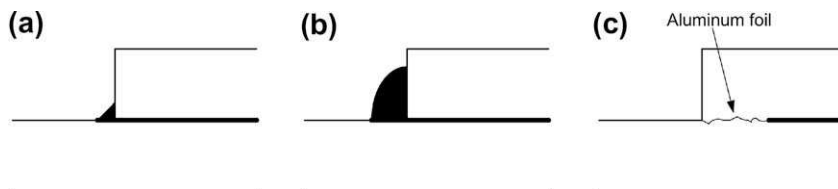


Fig. 7. Different overlap end conditions: (a) small fillet, (b) large fillet and (c) precracked.

than the other so that a higher bending moment was applied at the overlap end of the longer arm. This ensured that a crack initiated and grew from only one end of the joint.

In order to investigate the effect of initiation on the ultimate strength, three different conditions at the overlap ends were considered: a small adhesive fillet, a large adhesive fillet and a precracked condition. The small adhesive fillet was formed by removing the excess adhesive from the end of the overlap using a small spatula before curing. The large adhesive fillet was formed by not removing this excess adhesive prior to curing. The precracked condition was formed by embedding a piece of 20 μ m thick aluminum foil that had been folded over to make an unbonded double layer in the adhesive at the end of the overlap. The resulting conditions at the overlap end are schematically shown in Fig. 7.

In addition to the aluminum joints, six CLS and six SLS joints were bonded using 25.4 mm \times 19.05 mm (1" \times 3/4") AISI 4140 steel flat bars (Tables 4 and 5). AISI 4140 in this thickness did not yield during the fracture experiments. The steel joints were made with the same three conditions at the end of the overlap as were the aluminum joints.

All specimens were loaded to ultimate fracture on a servo-hydraulic load frame at a constant displacement rate. The crack initiation and growth were monitored during the loading of the specimen using a CCD camera with a high-magnification lens, giving a field of view of 3 mm. The camera was mounted on a motorized linear stage to follow the crack tip as it was advancing with increasing load. The measured force and crack length as a function of time were used to calculate the corresponding G . The video recording was also analyzed to identify the approximate crack initiation load.

As with the DCB joints, the fractures were entirely cohesive for the aluminum CLS and SLS joints, while the steel fracture surfaces were predominately cohesive with scattered, small patches of interfacial failure that covered about 20% of the total fracture surface.

Table 4

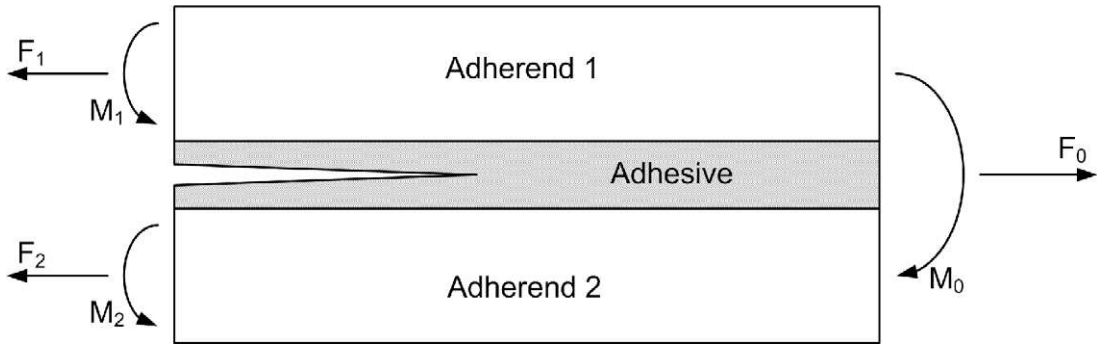
Geometry and initial conditions of steel CLS specimens, and comparison between the experimental, P_{Exp} , and predicted failure loads, P_{Pred} , per unit width. SF, LF and P stand for small fillet, large fillet and precracked, respectively.

Specimen, initial condition	L_1, L_2 (mm)	P_{Exp} (kK/m)	P_{Pred} (kN/m)	Error (%), $(P_{Pred} - P_{Exp})/P_{Exp}$
CLS 1B, SF	274, 183	5328	5540	4
CLS 2B, SF	349, 142	4471	4704	5
CLS 3A, SF	319, 170	4651	5228	12
CLS1A, LF	311, 141	4132	4720	14
CLS 2A, LF	227, 129	4540	4587	1
CLS 3B, P	277, 154	4677	4989	7

Table 5

Geometry and initial conditions of steel SLS specimens, and comparison between the experimental, P_{Exp} , and predicted failure loads, P_{Pred} , per unit width. SF, LF and P stand for small fillet, large fillet and precracked, respectively.

Specimen, initial condition	L_1, L_2, L_3 (mm)	P_{Exp} (kK/m)	P_{Pred} (kN/m)	Error (%), $(P_{Pred} - P_{Exp})/P_{Exp}$
SLS15A, SF	158, 173, 122	4313	4156	−4
SLS15C, SF	217, 107, 93	2923	2923	0
SLS14A, LF	159, 128, 82	3436	3223	−6
SLS14C, LF	138, 173, 102	4273	4097	−4
SLS14B, P	223, 141, 194	3685	4028	9
SLS15B, P	217, 87, 93	2473	2731	11

**Fig. 8.** Cracked adhesive sandwich model at the end of the overlap of SLS and CLS joints.

4.1. Data analysis, G calculation and mode partitioning of CLS and SLS joints

To calculate the energy release rate, an “adhesive sandwich” was isolated in the CLS and SLS joints as shown in Fig. 8, and the J -integral for this sandwich was calculated as [13]:

$$G = \left[\frac{F_1^2}{2(Eh)_1} + \frac{M_1^2}{2D_1} \right] + \left[\frac{F_2^2}{2(Eh)_2} + \frac{M_2^2}{2D_2} \right] - \left[\frac{F_0^2}{2(Eh)_0} + \frac{M_0^2}{2D_0} \right] \quad (15)$$

where F and M are, respectively, the tensile force and the bending moment per unit width in the adherends at the crack tip, while E and h are the elastic modulus and the beam thickness. Subscripts 1, 2 and 0 denote the respective cross-sections, as shown in Fig. 8. D is the flexural rigidity per unit width of the beam (Eq. (5)). Note that it is not necessary to assume the existence of a crack in the adhesive layer – if there is no crack, the strain energy release rate is calculated in the same way and represents the value for a crack just beginning to grow from the end of the overlap.

To calculate the tensile forces and bending moments acting at the ends of the adhesive sandwich element modeled by Eq. (15), the following equation for beam deflection, v , has been solved [15]:

$$\frac{\partial^4 v_i}{\partial x^4} - \frac{P}{D_i} \frac{\partial^2 v_i}{\partial x^2} = 0 \quad (16)$$

which has the general solution

$$v_i = C_{i1}x + C_{i2} + C_{i3} \cosh(\lambda_i x) + C_{i4} \sinh(\lambda_i x) \quad (17)$$

where

$$\lambda = \sqrt{\frac{P}{D_i}} \quad (18)$$

CLS and SLS joints are divided, respectively, into two and three beam sections denoted by the subscript, i . The constants, C_{i1} – C_{i4} , were determined using the boundary conditions together with the beam theory relations for bending moments and shear forces. At the loading pins, the transverse deflections and bending moments were considered to be zero. At the overlap ends, continuity implies that the displacements and slopes match for the two beam sections. For CLS joints, this yields eight linear equations in eight unknowns for which a closed-form solution exists [15,16]. For SLS joints, a set of 12 equations in 12 unknowns was solved numerically [15,16]. The Appendix gives the constants for the CLS joints and the set of equations for the SLS joints.

The phase angles for the CLS and SLS joints can be calculated by using the following expressions [15]:

$$G_I = \frac{[M_2(0^-)]}{4D_1} \quad (19)$$

$$G_{II} = G - G_I \quad (20)$$

$$|\psi| = \arctan \left(\sqrt{\frac{G_{II}}{G_I}} \right) \quad (21)$$

where $M_2(0^-)$ is the bending moment immediately to the left of the crack tip.

The G calculation and mode partitioning for the CLS and SLS joints presented above are based on beam theory, and to maintain consistency, the fracture envelope derived from beam theory (Eqs. (10) and (13)) for the aluminum and steel adhesive systems, respectively, was used to predict the ultimate fracture load in the CLS and SLS joints. As mentioned previously, the simpler beam theory model neglects the compliance of the adhesive layer and underestimates the strain energy release rate. However, simplifying the analysis using beam theory for both the fracture envelope DCB calculations and those for the actual CLS and SLS joints produces offsetting errors that have a small net effect on the ultimate fracture load prediction. This approach was successfully followed in Ref. [16]. Having calculated the phase angle, P_{pred} is the force that yields the critical strain energy release rate, G_c^s , from the fracture envelope at the calculated phase angle, ψ .

4.2. Experimental results and predictions

4.2.1. Aluminum adhesive system

As expected from the adhesive R -curve behavior, cracks started to propagate at loads between 30% and 90% of the ultimate failure load. The subcritical crack propagated in a stable manner for several centimeters before the ultimate critical load was attained and final fast fracture occurred. The measured crack initiation and final failure loads for the aluminum CLS and SLS joints with different initial conditions are given in Tables 2 and 3. Fig. 9 compares the approximate crack initiation strain energy release rate, G_c^i , with the corresponding steady-state critical strain energy release rate, G_c^s , for the CLS and SLS joints with the three different overlap end conditions. The given G_c^s for each specimen was the value at the ultimate load of the joint and was based on the phase angle calculation of the initial geometry of the specimen. As will be discussed below, this phase angle was only slightly different from the phase angle at the critical actual crack length corresponding to final rupture. It is clear that for all three overlap end conditions, the crack started propagating at significantly lower G_c^i values than the G_c^s . As mentioned before, this behavior is attributed to the damage zone development ahead of the crack tip, which occurred in the quasi-static loading of CLS and SLS joints as well as in the DCBs used to measure the fracture envelope.

Since crack initiation occurred well below the joint ultimate load and was followed by a period of stable crack growth, the ultimate fracture load did not depend on the initial condition at the end of the joint overlap (fillet or precrack), which is consistent with the results for the adhesive system of Ref. [17].

Phase angles that can be achieved by changing the geometry of CLS and SLS joints are in the relatively narrow range of 45° – 55° , as can be seen in Tables 2 and 3. Fig. 5 shows that the crack propagation associated with the rising part of the DCB R -curve for phase angles in this range was between 40 and 60 mm for aluminum specimens. This length corresponded to a change in the appearance of the fracture surfaces of the SLS and CLS joints, which displayed two distinct regions corresponding to slow, stable crack extension and then fast fracture. An example of this is shown in Fig. 10 for two of the SLS joints. For the tested CLS and SLS specimens this change in the failure surface occurred at an average of 60 ± 10 mm from point of crack initiation, which was approximately the length of crack growth seen during the rising part of the R -curve in DCB tests, implying that the SLS and CLS joints reached their ultimate strength and became unstable when the adhesive damage zone had fully developed at $G_c = G_c^s$. This crack growth pattern was confirmed using the CCD camera to monitor the crack length during CLS and SLS testing. As expected from the failure surface, after the crack initiated, it propagated stably with a gradually increasing crack speed from approximately 0.02 mm/s to about 0.35 mm/s under an increasing joint load until very close to the moment of final fracture when the crack speed increased sharply and the joint broke. The recorded crack length at the onset of fast fracture was consistent with the location of the change in the failure surface seen in Fig. 10.

Based on the optically measured crack lengths at different times during the SLS and CLS testing, the energy release rate was calculated for some of the specimens during the subcritical crack growth. Fig. 11 compares the G_c vs. crack length graphs obtained from a CLS joint with the corresponding graph obtained from DCB fracture envelope tests at $\psi = 55^\circ$. It should be noted that the phase angle generally decreases with increasing crack length in CLS specimens [15]; however, for the present specimens, this change in phase angle due to the subcritical crack growth was less than 5° . This small change in the phase angle with crack length results from the increase in L_1 and the corresponding decrease in L_2 (Fig. 1), and may be calculated

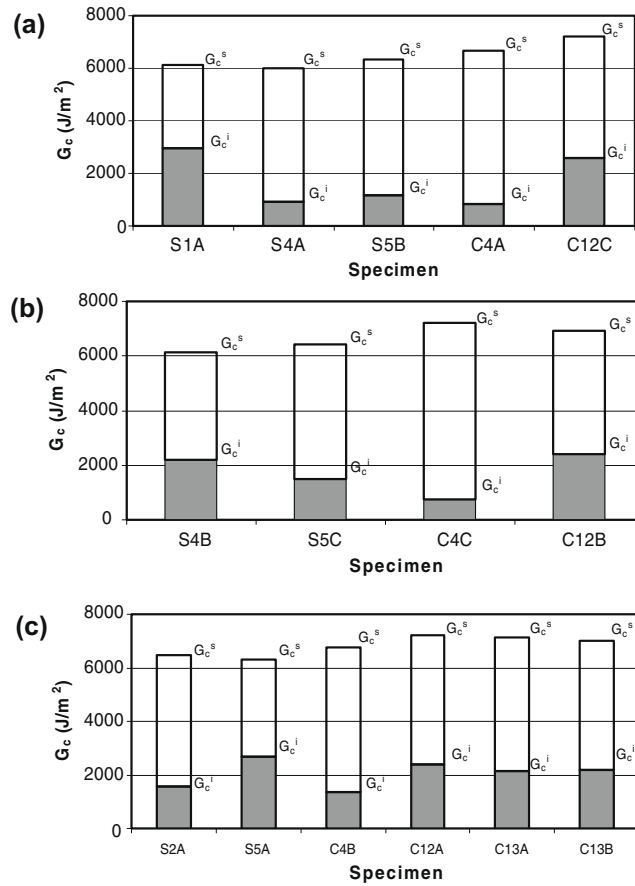


Fig. 9. Approximate crack initiation energy release rate, G_c^i (shaded) observed with aluminum CLS and SLS specimens compared with the steady-state critical strain energy release rate, G_c^s , from the fracture envelope at the same phase angle. CLS and SLS initial conditions: (a) small fillet, (b) large fillet and (c) precracked. Specimen numbers refer to Tables 2 and 3.

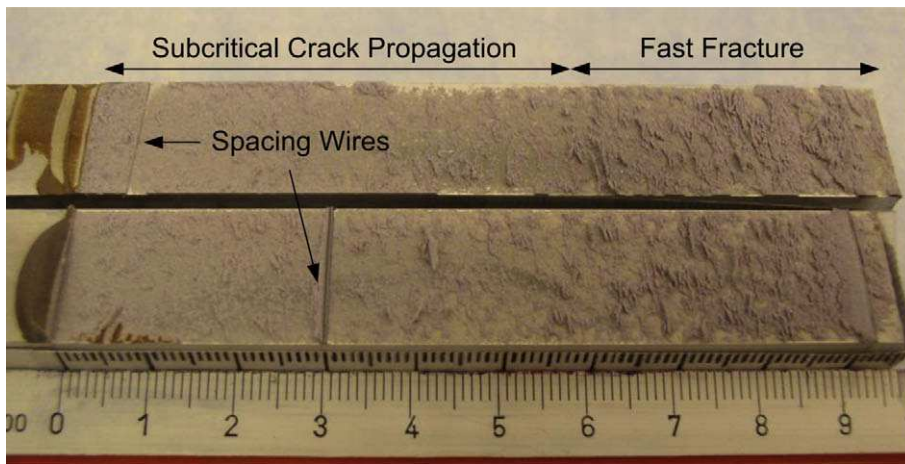


Fig. 10. Fracture surfaces of two different aluminum SLS joints. The crack initiated from the fillet at the left end of each overlap shown. Bondline spacing wires, as shown above, are at 5 mm and 30 mm in upper and lower joints, respectively.

using the equations in the Appendix for CLS joints. It is observed that the G_c vs. crack length graph obtained from a CLS joint was similar to the corresponding graph from a DCB joint at the same phase angle, and that the G_c for the CLS joint reached the plateau of the DCB graph at a crack length of 50–60 mm.

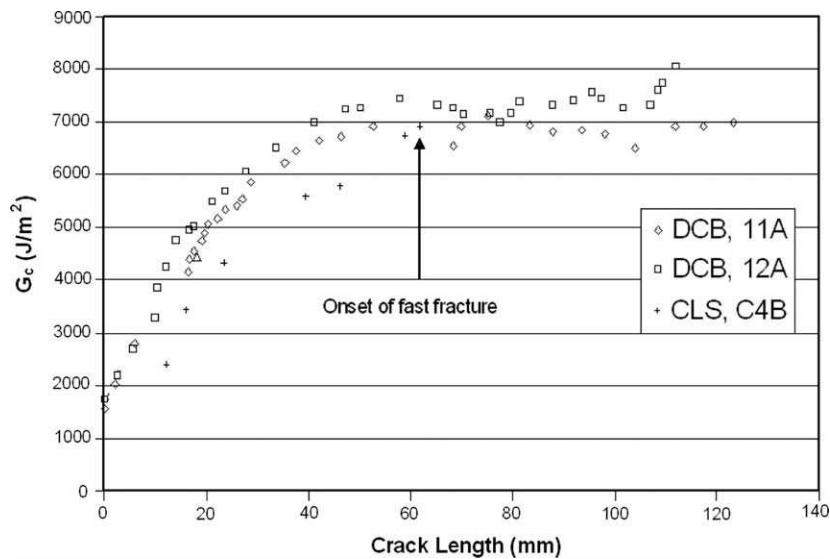


Fig. 11. Comparison of G_c vs. crack length for an aluminum CLS joint and two aluminum DCB fracture envelope tests at $\psi = 55^\circ$. Point of onset of fast fracture is shown for CLS joint.

Table 6

Sensitivity of the failure load predictions to the assumed subcritical crack growth length for aluminum CLS and SLS joints. Errors are between experimental and predicted failure loads. The average absolute error is the average of the absolute value of each error in the failure load predictions.

Subcritical crack growth length (mm)	0	40	50	60	70	80
<i>CLS joints (%)</i>						
Average error	23	2	−4	−8	−12	−17
Average absolute error	23	5	7	10	13	17
<i>SLS joints (%)</i>						
Average error	33	11	6	1	−3	−7
Average absolute error	33	11	6	4	5	7

In summary, the subcritical crack growth length was consistent with the location of the change in the fracture surface of CLS and SLS joints. It also agreed with the optically measured crack length at the onset of fast fracture, and was close to the length of the rising part of a DCB test at $\psi = 55^\circ$. Therefore, it is concluded that, as the crack grows and the applied G on the CLS or SLS joints is increased, G_c also increases due to the development of the damage zone. This toughening behavior prevents the joint from fracturing and the joint can bear higher forces. As the G_c reaches the plateau value, G_c^s , the toughening ends and catastrophic failure of the joint occurs. The subcritical crack growth length must therefore be considered when predicting the ultimate failure load using the fracture envelope.

Based on the above observations, the failure loads for the aluminum CLS and SLS joints were predicted by calculating the phase angle for the joint at the critical crack length and then using the fracture envelope (Fig. 6) to find the corresponding G_c^s . The ultimate joint strength was then the load that would generate such a strain energy release rate. For all of these SLS and CLS ultimate load predictions, it was assumed that the subcritical crack length was 60 mm. Tables 2 and 3 show that the measured ultimate loads and the predictions agreed well, with an average absolute relative error of 9% and 4%, respectively, for CLS and SLS joints.

In order to assess the sensitivity of the ultimate load prediction on the assumed amount of subcritical crack growth, predictions were also made assuming lengths of 0, 40, 50, 70 and 80 mm. The average relative error and the average absolute relative error between the predictions and experiments are given in Table 6 for CLS and SLS joints. It is seen that errors as large as 29% occurred if subcritical crack growth was not taken into account in the calculation of ψ and G_c , but that the failure load prediction was relatively insensitive to the amount of subcritical crack propagation assumed in the analysis; e.g. using a subcritical crack length of 40 mm or 80 mm instead of the actual subcritical crack length of 60 mm increased the average absolute error by less than 7% for both CLS and SLS joints. Therefore, choosing this subcritical crack length based on the length of the rising part of the R -curve in DCB fracture envelope tests for the corresponding phase angle yields good predictions of the final fracture load for CLS and SLS joints.

In earlier work with the relatively brittle Cybond 4532 GB adhesive [16,17], the rising part of the R -curve was only about 5 mm for phase angles of 45° – 55° , the range for CLS and SLS joints. Therefore, it was not necessary to base the ultimate load calculation of G_c on the joint geometry at the point of final failure. As a result, the ultimate load of SLS and CLS joints could be found by assuming that G_c^s was reached at the overlap end with no subcritical crack growth.

For most of the CLS and SLS fracture joints, the cross-head displacement was increased continuously until the final failure, but for two CLS and two SLS joints, a start–stop loading was followed, similar to that used with the DCB tests. In this approach, the displacement was increased at a constant slow rate until the crack started to grow. At this point the displacement was held constant until the crack arrested as G fell. This was followed by another increase in displacement until the crack again propagated, and the displacement was again held constant until the crack arrested. This quasi-static procedure was repeated until catastrophic failure occurred. For the chosen range of crack speed in our fracture experiments, no difference was observed in the amount of subcritical crack growth or the R -curve behavior of the adhesive compared with the continuous loading, and the experimental fracture load was still close to the predictions, with an average absolute error of 6%. Therefore, it was concluded that these forms of continuous and start–stop loading were sufficiently similar to produce the same G_c^s and length of the rising part of the R -curve.

4.2.2. Steel adhesive system

Tables 4 and 5 give the geometry of the steel CLS and SLS specimens, which were tested at a constant displacement rate of 0.25 mm/min.

For the steel CLS and SLS joints, the transition between slow stable crack propagation and the fast final fracture occurred at 70 ± 10 mm from the end of the overlap. As with the aluminum joints, this was consistent with the length of the rising part of the R -curve for steel DCB joints tested at the same phase angle. Tables 4 and 5 give the predicted ultimate loads for CLS and SLS tests, respectively, assuming 70 mm of subcritical crack growth. The agreement with the measured ultimate loads was good, having an average absolute error for CLS and SLS joints of 6% and 7%, respectively. As with the aluminum joints, the length of the subcritical crack growth in the CLS and SLS joints could be estimated to be the same as the length of the rising part of the R -curve in DCB fracture envelope tests.

A limitation of this approach to ultimate load prediction is that the overlap must be at least as long as the subcritical crack growth length—approximately 60 mm with aluminum CLS and SLS joints and 70 mm for the steel joints. The prediction of the ultimate load for shorter joints would require a more accurate model of subcritical crack growth; in particular, the critical strain energy release rate at initiation, G_c^i , and G_c vs. crack length in the rising part of the R -curve. Comparing this crack growth behavior with the calculated strain energy release rate at the particular phase angle of the joint would allow the prediction of the maximum attainable load.

5. Conclusions

A previously established fracture-based, analytical approach for predicting the ultimate loads in common adhesive joints (CLS and SLS) can be applied to an epoxy adhesive that is an order of magnitude tougher than the earlier generation of (untoughened) epoxy adhesives, provided the joint analysis takes into account the degree of subcritical crack growth. The approach is based on the observation that the strength of an adhesive bondline can be characterized by the fracture envelope for that particular adhesive system (i.e. the critical strain energy release rate, G_c , as a function of the mode ratio of loading, ψ). The subcritical crack growth length for both CLS and SLS specimens was approximately equal to the length of the rising part of the R -curve from the DCB specimens used to measure the fracture envelope. Using this approach, the average absolute error in the ultimate strength predictions was less than 10% for both aluminum and steel CLS and SLS joints.

The joint strength increased as the elastic modulus of the adherend increased as seen when comparing the steel and aluminum joints. This was simply due to the relation between load, stiffness and the strain energy release rate. However, no difference was observed in the critical strain energy release rates that could be attributed to the adherend modulus.

Although the approach has been demonstrated for SLS and CLS joints of aluminum and steel, it is also applicable to other elastically deforming two-dimensional joint such as double lap joints. A “sandwich element” is isolated from the overlap end of the joint, and the force and moment reactions acting on the sandwich are used to calculate the strain energy release rate and the phase angle of loading.

During the fracture envelope measurement using aluminum and steel DCB specimens, the toughening behavior of the adhesive produced a relatively long rising part of the R -curve (G_c vs. crack length) prior to reaching a steady-state critical strain energy release rate, G_c^s . This extensive, stable subcritical crack growth also occurred during the loading of the CLS and SLS joints, thereby changing the joint geometry considerably and altering the strain energy release rate, G , and to a smaller extent, the crack tip mode ratio, ψ . It was found that accurate predictions of the ultimate load could be made if ψ and G are calculated using the final geometry of the CLS and SLS joints after subcritical crack growth equal to that observed in the DCB fracture tests. It was shown that the prediction of the ultimate load is relatively insensitive to the assumed amount of subcritical crack growth. As well, because the subcritical crack growth was so large, the ultimate joint strength was independent of the geometry of the end of the joint overlap (e.g. fillet shape). The detailed geometry of the end of the adhesive layer is expected to affect only the crack initiation load.

Due to the R -curve behavior of the adhesive, the method can only be used to predict the ultimate load of joints having an overlap at least as large as the average subcritical crack growth length; otherwise the adhesive crack tip damage zone will not correspond to G_c^s . For joints with shorter overlaps, the rising part of the R -curve behavior would need to be modeled to permit a failure criterion based on G_c as a function of the subcritical crack length, rather than the steady-state value G_c^s . Another limitation of the present approach is that it is applicable only to elastically deforming adherends since the equations

used to calculate the strain energy release rate and the phase angle are based on this assumption, and the fracture envelope (G_c as a function of the phase angle) was measured using elastic DCB specimens.

The high toughness and visco-elastic nature of the adhesive made it preferable to identify the critical fracture load during the DCB fracture envelop testing using load drop rather than the earlier optical method of detecting crack advance. These DCB fracture tests were relatively insensitive to the cross-head speed over the range 0.5–5 mm/min.

Acknowledgements

The authors acknowledge the Natural Sciences and Engineering Research Council of Canada, the Ontario Centers of Excellence, and General Motors of Canada for their financial support. The second author wishes to acknowledge NRC Aluminum Technology Center for financial support.

Appendix A

The equations that are used to calculate the energy release rate, G , and phase angle, ψ , from the calculation of beam deflections are presented in this appendix.

A.1. CLS joints

Following the approach in Ref. [15], a CLS joint is divided into two beams, and for each, the beam deflection is assumed according to Eq. (17). Applying the boundary conditions, the continuity of displacements and slopes for the overlap end, and considering that the difference in bending moments at the right and left side of the overlap end must be the moment due to the tensile force, together with the beam theory relations for bending moments and shear forces, eight equations were derived. Solving these set of equations, yielded the following closed-form solution for the constants in the beam deflection solution (Eq. (17)):

$$C_3 = -\frac{P\Delta\lambda_2}{D_1\lambda_1^2} \left(\frac{\tanh(-\lambda_1 L_1)}{\lambda_2 \tanh(-\lambda_1 L_1) - \lambda_1 \tanh(-\lambda_2 L_2)} \right) \quad (A.1)$$

$$C_4 = -\frac{P\Delta\lambda_2}{D_1\lambda_1^2} \left(\frac{1}{\lambda_2 \tanh(-\lambda_1 L_1) - \lambda_1 \tanh(-\lambda_2 L_2)} \right) \quad (A.2)$$

$$C_7 = -\frac{P\Delta\lambda_1}{D_2\lambda_2^2} \left(\frac{\tanh(\lambda_2 L_2)}{\lambda_2 \tanh(-\lambda_1 L_1) - \lambda_1 \tanh(-\lambda_2 L_2)} \right) \quad (A.3)$$

$$C_8 = -\frac{P\Delta\lambda_1}{D_2\lambda_2^2} \left(\frac{1}{\lambda_2 \tanh(-\lambda_1 L_1) - \lambda_1 \tanh(-\lambda_2 L_2)} \right) \quad (A.4)$$

$$C_2 = \frac{L_1 L_2}{L_1 + L_2} \left(\frac{C_7 - C_3}{L_2} + C_8 \lambda_2 - C_4 \lambda_1 \right) \quad (A.5)$$

$$C_1 = \frac{C_2}{L_1} \quad (A.6)$$

$$C_6 = C_2 + C_3 - C_7 \quad (A.7)$$

$$C_5 = -\frac{C_6}{L_2} \quad (A.8)$$

where $\Delta = h/2$ (h being the thickness of adherends).

Having the beam deflection, the bending moments at any desired cross-section of $x = x_c$, x was measured from the overlap end in Fig. 1, and could be calculated by:

$$M = -D \frac{\partial^2 v(x_c)}{\partial x^2} \quad (A.9)$$

The crack tip is at $x = 0$. G was calculated from Eq. (15), and for phase angle, Eqs. (19)–(21) were used. This will lead to the following equations for equal-adherend CLS joints [15]:

$$G = Eh^5 \lambda_1^4 \left(\frac{1}{576} + \frac{\tanh^2(\lambda_1 L_1) - \tanh^2(\lambda_2 L_2)}{768 [\sqrt{1/8} \tanh(\lambda_1 L_1) + \tanh(\lambda_2 L_2)]^2} \right) \quad (A.10)$$

$$\frac{G_{II}}{G_I} = \frac{4}{3} + \frac{4}{3} \sqrt{2} \left(\frac{\tanh(\lambda_2 L_2)}{\tanh(\lambda_1 L_1)} \right) + \frac{2}{3} \left(\frac{\tanh(\lambda_2 L_2)}{\tanh(\lambda_1 L_1)} \right)^2 \quad (A.11)$$

$$|\psi| = \arctan \left(\sqrt{\frac{G_{II}}{G_I}} \right) \quad (A.12)$$

A.2. SLS joints [15]

The approach for calculating the beam deflections and, therefore, the bending moments, for SLS joints was similar to the approach explained above for CLS geometry. However, instead of two beam sections for the case of CLS, the SLS joint is divided into three beams. This will lead to 12 equations and 12 unknowns. This set of equations is presented below, and was solved numerically to find the beam deflection constants. For simplicity, in the following equations L_1 is as illustrated in Fig. 1, however, $L_2 = (L_1 + L_2)$ Fig. 1 and $L_3 = (L_1 + L_2 + L_3)$ Fig. 1.

$$C_2 = C_3 = 0 \quad (\text{A.13})$$

$$C_1 L_1 + C_4 \sinh(\lambda_1 L_1) = C_5 L_1 + C_6 + C_7 \cosh(\lambda_2 L_1) + C_8 \sinh(\lambda_2 L_1) \quad (\text{A.14})$$

$$C_1 + C_4 \lambda_1 \cosh(\lambda_1 L_1) = C_5 + C_7 \lambda_2 \sinh(\lambda_2 L_1) + C_8 \lambda_2 \sinh(\lambda_2 L_1) \quad (\text{A.15})$$

$$-D_1 C_4 \lambda_1^2 \sinh(\lambda_1 L_1) - P \Delta_1 = -D_2 \lambda_2^2 [C_7 \cosh(\lambda_2 L_1) + C_8 \sinh(\lambda_2 L_1)] \quad (\text{A.16})$$

$$-D_1 C_4 \lambda_1^3 \cosh(\lambda_1 L_1) = -D_2 \lambda_2^3 [C_7 \sinh(\lambda_2 L_1) + C_8 \cosh(\lambda_2 L_1)] \quad (\text{A.17})$$

$$C_5 L_2 + C_6 + C_7 \cosh(\lambda_2 L_2) + C_8 \sinh(\lambda_2 L_2) = C_9 L_2 + C_{10} + C_{11} \cosh(\lambda_3 L_2) + C_{12} \sinh(\lambda_3 L_2) \quad (\text{A.18})$$

$$C_5 + C_7 \lambda_2 \sinh(\lambda_2 L_2) + C_8 \lambda_2 \cosh(\lambda_2 L_2) = C_9 + C_{11} \lambda_3 \sinh(\lambda_3 L_2) + C_{12} \lambda_3 \cosh(\lambda_3 L_2) \quad (\text{A.19})$$

$$-D_2 \lambda_2^2 [C_7 \cosh(\lambda_2 L_2) + C_8 \sinh(\lambda_2 L_2)] - P \Delta_2 = -D_3 \lambda_3^2 [C_{11} \cosh(\lambda_3 L_2) + C_{12} \sinh(\lambda_3 L_2)] \quad (\text{A.20})$$

$$-D_2 \lambda_2^3 [C_7 \sinh(\lambda_2 L_2) + C_8 \cosh(\lambda_2 L_2)] = -D_3 \lambda_3^3 [C_{11} \sinh(\lambda_3 L_2) + C_{12} \cosh(\lambda_3 L_2)] \quad (\text{A.21})$$

$$C_9 L_3 + C_{10} + C_{11} \cosh(\lambda_3 L_3) + C_{12} \sinh(\lambda_3 L_3) = 0 \quad (\text{A.22})$$

$$C_{11} \cosh(\lambda_3 L_3) + C_{12} \sinh(\lambda_3 L_3) = 0 \quad (\text{A.23})$$

where $\Delta_1 = \Delta_2 = h/2$. The set of coordinates originated at the left loading pin in Fig. 1.

Knowing the bending moments at the crack tip, $M_1(L_1^-)$ and $M_2(L_1^+)$, Eq. (15) reduces to:

$$G = \left[\frac{M_1^2(L_1^-)}{2D_1} + \frac{P^2}{2(Eh)_1} \right] - \left[\frac{M_2^2(L_1^+)}{2D_2} + \frac{P^2}{2(Eh)_2} \right] \quad (\text{A.24})$$

For the SLS joints with equal adherends, which was the case in this study, the phase angle was calculated as follows:

$$G_I = \frac{M_1(L_1^-)^2}{4D_1} \quad (\text{A.25})$$

$$G_{II} = G - G_I \quad (\text{A.26})$$

$$|\psi| = \arctan \left(\sqrt{\frac{G_{II}}{G_I}} \right) \quad (\text{A.27})$$

References

- [1] Harris JA, Adams RD. Strength prediction of bonded single lap joints by non-linear finite element methods. *Int J Adhes Adhes* 1984;4(2):65–78.
- [2] Czamocki P, Piekarski K. Fracture strength of an adhesive-bonded joint. *Int J Adhes Adhes* 1986;6(2):93–5.
- [3] Adams RD. Strength predictions for lap joints, especially with composite adherends. A review. *J Adhes* 1989;30(1):219–42.
- [4] Lee SJ, Lee DG. Development of a failure model for the adhesively bonded tubular single lap joint. *J Adhes* 1992;40(1):1–14.
- [5] Feih S, Shercliff HR. Adhesive and composite failure prediction of single-L joint structures under tensile loading. *Int J Adhes Adhes* 2005;25(1):47–59.
- [6] Soutis C, Duan D-M, Goutas P. Compressive behaviour of CFRP laminates repaired with adhesively bonded external patches. *Compos Struct* 1999;45(4):289–301.
- [7] Sheppard A, Kelly D, Tong L. A damage zone model for the failure analysis of adhesively bonded joints. *Int J Adhes Adhes* 1998;18(6):385–400.
- [8] Ban C-S, Lee Y-H, Kwon J-H. Strength prediction of adhesive joints using the modified damage zone theory. *Compos Struct* 2008;86(1–3):96–100.
- [9] Liljedahl CDM, Crocombe AD, Wahab MA, Ashcroft IA. Damage modelling of adhesively bonded joints. *Int J Fract* 2006;141:147–61.
- [10] Kafkalidis MS, Thouless MD. The effects of geometry and material properties on the fracture of single lap-shear joints. *Int J Solids Struct* 2002;39:4367–83.
- [11] Sun C, Thouless MD, Waas AM, Schroeder JA, Zavattieri PD. Ductile–brittle transitions in the fracture of plastically deforming, adhesively bonded structures. Part II: numerical studies. *Int J Solids Struct* 2008;45:4725–38.
- [12] Jensen HM. Interface fracture in adhesively bonded shell structures. *Eng Fract Mech* 2008;75(3–4):571–8.
- [13] Fernlund G, Spelt JK. Failure load prediction of structural adhesive joints. Part 1: analytical method. *Int J Adhes Adhes* 1991;11(4):213–20.
- [14] Fernlund G, Spelt JK. Mixed-mode fracture characterization of adhesive joints. *Comp Sci Technol* 1994;50(4):441–9.
- [15] Papini M, Fernlund G, Spelt JK. The effect of geometry on the fracture of adhesive joints. *Int J Adhes Adhes* 1994;14(1):5–13.
- [16] Fernlund G, Papini M, McCammond D, Spelt JK. Fracture load predictions for adhesive joints. *Comp Sci Technol* 1994;51(4):587–600.
- [17] Papini M, Fernlund G, Spelt JK. Effect of crack-growth mechanism on the prediction of fracture load of adhesive joints. *Comp Sci Technol* 1994;52(4):561–70.
- [18] Wegman RF. Surface preparation techniques for adhesive bonding. New Jersey: Noyes Publications; 1989.
- [19] Fernlund G, Spelt JK. Mixed mode energy release rates for adhesively bonded beam specimens. *J Comp Tech Res* 1994;16(3):234–43.
- [20] Hutchinson JW, Suo Z. Mixed mode cracking in layered materials. In: Hutchinson JW, Wu TY, editors. *Advances in applied mechanics*, vol. 29. New York: Academic Press Inc.; 1992. p. 63–191.
- [21] Reimann IE, Dalgleish BJ, Evans AG. The fracture resistance of a model metal/ceramic interfaces. *Acta Metall Mater* 1991;39(12):3133–41.
- [22] Spearing SM, Evans AG. The role of fiber bridging in the delamination resistance of fiber-reinforced composites. *Acta Metall Mater* 1992;40(9):2191–9.
- [23] Suo Z, Bao G, Fan B. Delamination R-curve phenomenon due to damage. *J Mech Phys Solids* 1992;40(1):1–16.

- [24] Tamuzs V, Tarasovs S, Vilks U. Progressive delamination and fiber bridging modeling in double cantilever beam composite specimens. *Eng Fract Mech* 2001;68:513–25.
- [25] Jacobsen TK, Sorenson BF. Mode I intra-laminar crack growth in composites-modelling of *R*-curves from measured bridging laws. *Compos: Part A* 2001;32:1–11.
- [26] Madhusudhana KS, Narasimhan R. Experimental and numerical investigations of mixed mode crack growth resistance of a ductile adhesive joint. *Eng Fract Mech* 2002;69:865–83.
- [27] Imanaka M, Motohashi M, Nishi K, Nakamura Y, Kimoto M. Crack-growth behavior of epoxy adhesives modified with liquid rubber and cross-linked rubber particles under mode I loading. *Int J Adhes Adhes* 2009;29:45–55.
- [28] Fleck NA, Hutchinson JW, Suo Z. Crack path selection in a brittle adhesive layer. *Int J Solids Struct* 1991;27(13):1683–703.
- [29] Xu XX, Crocombe AD, Smith PA. Mixed-mode fatigue and fracture behaviour of joints bonded with either filled or filled and toughened adhesive. *Int J Fatigue* 1995;17(4):279–86.
- [30] Yan C, Mai YW, Yuan Q, Ye L, Sun J. Effects of substrate materials on fracture toughness measurements in adhesive joints. *Int J Mech Sci* 2001;43:2091–102.
- [31] Bell AJ, Kinloch AJ. The effect of the substrate material on the value of the adhesive fracture energy. *J Mater Sci Lett* 1997;16:1450–3.
- [32] Blackman BRK, Kinloch AJ, Paraschi M. The effect of the substrate material on the value of the adhesive fracture energy, G_c : further considerations. *J Mater Sci Lett* 2001;20:265–7.